Numerical evaluation of three non-coaxial kinematic models using the distinct element method for elliptical granular materials: Numerical Evaluation of Three non-Coaxial Kinematic...

Article *in* International Journal for Numerical and Analytical Methods in Geomechanics · January 2016

Impact Factor: 1.38 · DOI: 10.1002/nag.2540

3 authors, including:

Mingjing Jiang

Tongji University

216 PUBLICATIONS **1,642** CITATIONS

SEE PROFILE

Marcos Arroyo

Polytechnic University of Catalonia

88 PUBLICATIONS **348** CITATIONS

SEE PROFILE

INTERNATIONAL JOURNAL FOR NUMERICAL AND ANALYTICAL METHODS IN GEOMECHANICS
Int. J. Numer. Anal. Meth. Geomech. (2016)
Published online in Wiley Online Library (wileyonlinelibrary.com). DOI: 10.1002/nag.2540

Numerical evaluation of three non-coaxial kinematic models using the distinct element method for elliptical granular materials

M. J. Jiang[1,2,3,*,†], J. D. Liu[1] and M. Arroyo[4]

[1]*Department of Geotechnical Engineering, Tongji University, Shanghai 200092, China*
[2]*State Key Laboratory of Disaster Reduction in Civil Engineering, Tongji University, Shanghai 200092, China*
[3]*Key Laboratory of Geotechnical and Underground Engineering of Ministry of Education, Tongji University, 1239 Siping Road, Shanghai 200092, China*
[4]*Department of Geotechnical Engineering and Geosciences, UPC, Barcelona, Spain*

SUMMARY

This paper presents a numerical evaluation of three non-coaxial kinematic models by performing Distinct Element Method (DEM) simple shear tests on specimens composed of elliptical particles with different aspect ratios of 1.4 and 1.7. The models evaluated are the double-shearing model, the double-sliding free-rotating model and the double slip and rotation rate model (DSR^2 model). Two modes of monotonic and cyclic simple shear tests were simulated to evaluate the role played by the inherent anisotropy of the specimens. The main findings are supported by all the DEM simple shear tests, irrespective of particle shape, specimen density or shear mode. The evaluation demonstrates that the assumption in the double-shearing model is inconsistent with the DEM results and that the energy dissipation requirements in the double-sliding free-rotating model appear to be too restrictive to describe the kinematic flow of elliptical particle systems. In contrast, the predictions made by the DSR^2 model agree reasonably well with the DEM data, which demonstrates that the DSR^2 model can effectively predict the non-coaxial kinematic behavior of elliptical particle systems. Copyright © 2016 John Wiley & Sons, Ltd.

Received 2 March 2014; Revised 6 April 2016; Accepted 26 April 2016

KEY WORDS: non-coaxial kinematic models; numerical simulations; elliptical particles; discrete element method

1. INTRODUCTION

Non-coaxiality, defined as the deviation of the principal plastic strain increment direction from the principal stress direction, is an important feature of granular material. It has been demonstrated [1–13] that non-coaxiality plays a key role in the fundamental mechanical behavior of geo-materials and in many geotechnical engineering problems that involve the rotation of the principal stresses. Hence, non-coaxiality should be considered when developing plasticity models for granular material [14–16]. Starting from the kinematic theory, various plasticity models have been proposed to describe 'fully developed' planar plastic flow of granular material. There are two outstanding features of these kinematic models: (i) they are formulated by defining the velocity field with several kinematic equations and (ii) they take the non-coaxiality of granular material into account. The most well-known kinematic models include the double-shearing model [17], the double-sliding free-rotating model [18] and the double slip and rotation rate model (DSR^2 model) [19]. These models describe the plastic flow of granular materials with several simple kinematic equations. If a

*Correspondence to: Mingjing Jiang, Department of Geotechnical Engineering, Tongji University, Shanghai 200092, China.
†E-mail: mingjing.jiang@tongji.edu.cn

single angular velocity Ω is introduced to describe the rotation rate of granular materials undergoing plastic flow, a unified formulation of these kinematic models can be obtained [20]. This indicates that the differences between these models lie in the choice of the angular velocity Ω, which will be discussed in Section 3. Briefly, the double-shearing model [17] employs the rotation rate of the principal stresses as the angular velocity; the double-sliding free-rotating model adopts the rotation rate of sliding elements as the angular velocity [18] and then the energy dissipation is assumed to be non-negative in each slip direction [21]; the DSR^2 model [19] introduces a quantity termed as the averaged pure rotation rate (APR) as the angular velocity. Therefore, all these kinematic models describe the non-coaxial macroscopic plastic flow by considering the deviation between the strain rate tensor and the principal stress tensor. Although all this models have a rational micromechanical basis, it is necessary to evaluate their ability to characterize non-coaxial plastic flow.

Constitutive models are usually evaluated by being compared with experimental data. However, experimental evaluation of the above kinematic models is extremely difficult because of the technical difficulty in measuring the key variables in physical experiments. For example, the APR in the DSR^2 model [19] is related to the rotation of contacting particles, which is difficult to measure in the laboratory with current technology. Hence, the Distinct Element Method (DEM) proposed by Cundall and Strack [22], which has been widely used to investigate the microscopic and macroscopic mechanical behavior [23–28] and boundary-value problems [29–32] of granular materials, is an appropriate method to perform such evaluations.

DEM has already been used to investigate the non-coaxial behavior of granular material [33–36]. However, only in the work of Jiang et al. [37] has DEM been used specifically to evaluate kinematic models for granular material undergoing non-coaxial flow. Jiang et al. [37] examined the abovementioned kinematic models by simulating monotonic and cyclic simple shear tests on assemblies of circular particles. It was concluded that (i) the angular velocity in the double-shearing model [17] is inconsistent with the DEM observations, (ii) the energy dissipation requirement in the double-sliding free-rotating model [21] is unduly restrictive and (iii) the APR in the DSR^2 model [19] correctly represented the rotation rate of granular material undergoing plastic flow. It is known, however, that non-circular particle shape has a significant effect on the behavior of granular material and, in particular, on the ability of particles to rotate [38–41]. A question now arises: are these conclusions [37] valid for non-circular particle assemblies? This question provides the motivation for the present study.

This paper evaluates the kinematic models for the non-coaxial plastic flow of assemblies of elliptical particles. The original DEM code NS2D [27–29] was modified to model elliptical particles. Using the modified NS2D, the double-shearing model, the double-sliding free-rotating model and the DSR^2 model are examined by performing strain-controlled monotonic and cyclic simple shear tests. In the simulations, specimens with different aspect ratios are used to obtain a convincing conclusion. In addition, all the specimens are subjected to two different modes of simple shear to check whether or not the inherent anisotropy influences the conclusions. Although DEM can also be used to investigate the reasons for non-coaxiality at the microscopic scale and how the micromechanical behavior creates the macroscopic response of the granular material, these aspects are out of the scope of the present work and will be the subject of future studies.

2. DEM TESTS ON ELLIPTICAL GRANULAR MATERIALS

2.1. Materials

The original DEM code, NS2D [27–29], was further improved for this investigation. The key improvements are in the detection of inter-particle or particle–wall contacts and the definition of the average pure rotation (APR) for elliptical particles. The algorithms proposed in [42] were used for the contact detection. The definition of APR for elliptical particles will be discussed in Section 3.4.

With the improved NS2D, DEM tests were carried out using elliptical particles with the equivalent particle size distribution shown in Figure 1. The equivalent particle size is defined as $d = \sqrt{d_a d_b}$,

DOI: 10.1002/nag

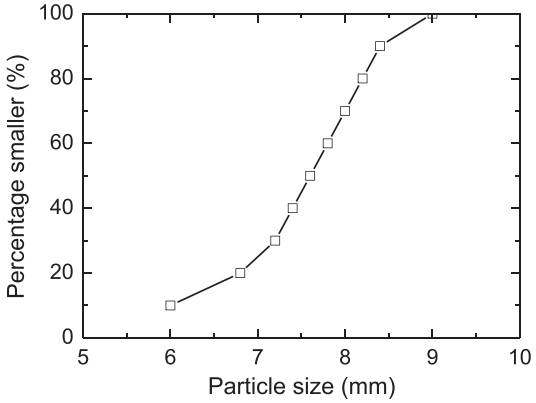

Figure 1. Grain size distribution of simulated granular material.

where d_a and d_b are the lengths of the major and minor axes of an elliptical particle, respectively. As shown in Figure 1, the equivalent particle size lies in the range between 6.0 mm and 9.0 mm, with the mean diameter $d_{50}=7.6$ mm. The aspect ratio defined as $A_m=d_a/d_b$ is another characteristic of an elliptical particle. In the DEM tests, two aspect ratios have been used, $A_m=1.4$ and 1.7, which are typical of two granular materials used in laboratory tests. Despite the same distribution of equivalent particle size, the specimens behave differently because of the difference in particle aspect ratio.

The double-shearing model [17] and the double-sliding free-rotating model [18] were originally proposed for non-dilatant materials and then extended for ideal dilatant materials to consider shear dilatancy. Because the evaluation will become unnecessarily complicated if volume change is considered, these kinematic models will be evaluated based on simulations in which the specimens do not change volume. Loose, medium-dense and dense specimens, are studied in parallel to obtain reliable conclusions. Table I summarizes the parameters used in the DEM simulations. Each numerical specimen had a total of 2032 elliptical particles surrounded by four rigid walls. The numerical specimens were prepared using the under-compaction multi-layer technique (UCM) [43]. The inter-particle and particle–wall contact law can be expressed as

$$\begin{cases} F_n = \max(k_n u_n, 0.0) \\ F_s = \min(k_s u_s, \mu F_n) \end{cases} \tag{1}$$

where k_n and k_s are the normal and tangential contact stiffnesses, u_n and u_s are the normal and tangential relative displacements and μ is the friction coefficient. All the particles were frictional with a coefficient of 0.5 while the walls were frictionless during specimen preparation. In addition, global damping was used to obtain quasi-static simulations under the given strain rate.

Table I. Parameters of the materials and simple shear tests in the DEM verifications.

Material parameters	
Specimen size (mm × mm)	About 325 × 340
Total number of particles	2032
Density of particles (kg/m^3)	2600
Particle aspect ratio (A_m)	1.4 and 1.7
Normal/tangential spring stiffness (N/m)	1.5×10^9, 1.0×10^9
Inter-particle friction coefficient	0.5
Planar void ratio (dense, medium-dense, loose)	0.16, 0.19, 0.22
Shear test parameters	
Initial rotation rate $.\theta_0$ (rad/min)	0.5 (monotonic test) 0.15 (cyclic test)
Period in cyclic simple shear test T(s)	120
Incremental time Δt (s)	1.0×10^{-4}

DOI: 10.1002/nag

2.2. Test program

The DEM tests include the compression and simple shear stages. In the compression stage, the specimens were vertically compressed under a pressure of 200 or 400 kPa with the two lateral walls fixed. In this stage, all the four rigid walls were assumed frictionless, and thus the major and minor principal stresses were perfectly vertical and horizontal, respectively. In the subsequent shear stage, all the rigid walls were frictional and the particle–wall friction coefficient was set to 0.5 to allow simple shearing. Note that the rough wall by itself may not necessarily create non-coaxiality. For example, non-coaxiality is hardly observed before strain localization occurs in biaxial tests. Hence, the simple shear tests described below were performed, which means that the non-coaxiality studied in this paper occurs because of shearing. In addition, the shear tests were performed in strain rate control mode rather than stress control mode. This is because (i) stress control shear tests require a highly-efficient servo-control mechanism, which makes the stress control shear tests far more complicated than the strain control tests in either laboratory tests or numerical simulations, and (ii) the strain softening cannot be observed in stress controlled laboratory tests or numerical simulations.

In the shear stage, the specimens were subjected to either monotonic or cyclic simple shearing in which the volume was kept constant. Because there was usually a preferred orientation of particle contacts or of the major particle axes in an assembly of elliptical particles, all the specimens generally exhibited a significant inherent anisotropy before the simple shear stage. It is known that inherent anisotropy usually plays an important role in the mechanical behavior of geomaterials [44–46]. Hence, all the specimens were loaded in two different modes during the simple shear stage, as shown in Figure 2, to account for the possible effect of inherent anisotropy. The first shear mode (Mode I) is when the two lateral walls rotate at the rate $\dot{\theta}$ while the top and bottom walls are vertically fixed but move horizontally at a rate of $\dot{\theta}\cdot h/2.0$, where h is the specimen height. The second shear mode (Mode II) is when the top and bottom walls rotate at a rate $\dot{\theta}$ while the two lateral walls are horizontally fixed but move vertically at a rate of $\dot{\theta}\cdot w/2.0$, where w is the specimen width. The rotation rate $\dot{\theta}$ is constant in the monotonic shear tests and periodic in the cyclic shear tests, as expressed by

$$\dot{\theta} = \begin{cases} \dot{\theta}_0, & \text{in monotonic shear tests} \\ \dot{\theta}_0 \cos\left(\dfrac{2\pi t}{T}\right), & \text{in cyclic shear tests} \end{cases} \tag{2}$$

where $\dot{\theta}_0$ is the maximum rotation rate, T is the rotation period and t is the current time. The rotation rate is taken as positive when the wall rotates counterclockwise.

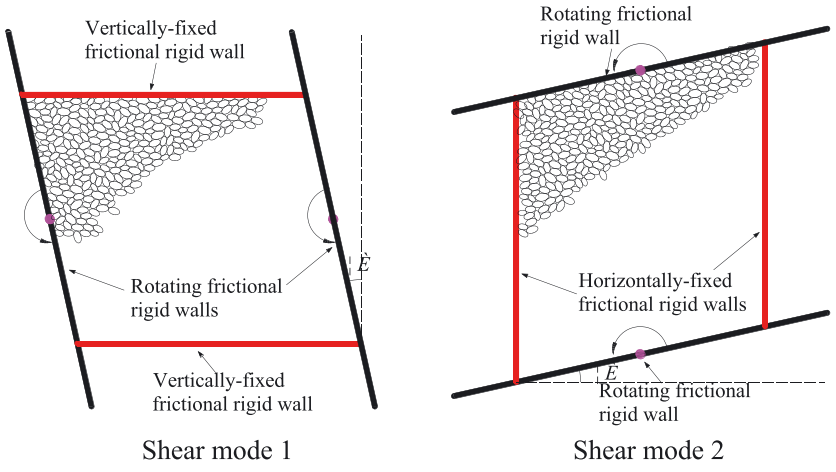

Figure 2. Shear modes of DEM simple shear tests.

DOI: 10.1002/nag

During the DEM tests, the velocity of a particle can be computed by the displacement increment over the corresponding time interval. In the simple shear tests, the distribution of the average velocity can be theoretically obtained. In Mode I simple shear test, the theoretical solution is given by

$$\begin{pmatrix} v_x \\ v_y \end{pmatrix} = \begin{pmatrix} -\dot{\theta}\cdot y \\ 0 \end{pmatrix} \tag{3a}$$

where y is the y-ordinate value of the given point. In Mode II simple shear test, the theoretical solution is given by

$$\begin{pmatrix} v_x \\ v_y \end{pmatrix} = \begin{pmatrix} 0 \\ \dot{\theta}\cdot x \end{pmatrix} \tag{3b}$$

where x is the x-ordinate value of the given point. The theoretical solutions given by Eq. (3a) and Eq. (3b) will be used to establish the evaluation criteria for the kinematic models, as discussed in Section 3. Moreover, the theoretical solutions can also serve as the benchmark to verify the DEM simple shear tests, as shown in Subsection 4.1.

Table I provides the parameters for the DEM simple shear tests. For each shear mode described above, eight undrained simple shear tests were performed: two monotonic shear tests on dense and loose specimens, one monotonic shear test on a medium-dense specimen and one cyclic shear test on dense, medium-dense and loose specimens. Therefore, a total of 32 simple shear tests were simulated. The maximum shear strain in the monotonic simple shear tests is chosen to be 18%, which is large enough to evaluate the abovementioned kinematic models. The same time increments were chosen for all the tests. The time increment was small enough that the specimens were always at quasi-static equilibrium during the simple shear tests.

3. EVALUATION CRITERIA FOR THE KINEMATIC MODELS

Evaluation criteria, by which the theoretical results obtained from the kinematic models can be compared with the DEM data, have been described in detail in the previous work dealing with circular granular materials [37]. For completeness and readability, these evaluation criteria will be briefly introduced below, as well as the modifications made for elliptical particles.

The velocity field for granular material undergoing planar flow can be described by the unified kinematic equations as follows [20]:

$$\begin{aligned} (d_{11}+d_{22})\cos\left(\frac{\varsigma+\xi}{2}\right) &= [(d_{11}-d_{22})\cos 2\psi_\sigma + 2d_{12}\sin 2\psi_\sigma]\sin\left(\frac{\varsigma-\xi}{2}\right) \\ 2(\Omega+w_{12})\sin\left(\frac{\varsigma+\xi}{2}\right) &= [(d_{11}-d_{22})\sin 2\psi_\sigma - 2d_{12}\cos 2\psi_\sigma]\cos\left(\frac{\varsigma-\xi}{2}\right) \end{aligned} \tag{4}$$

where ς and ξ are material parameters, Ω is the angular velocity, the deformation rate $d_{ij} = \frac{1}{2}\left(\frac{\partial v_i}{\partial x_j} + \frac{\partial v_j}{\partial x_i}\right)$ and the spin tensor $w_{ij} = \frac{1}{2}\left(\frac{\partial v_i}{\partial x_j} - \frac{\partial v_j}{\partial x_i}\right)$ with v_i being the velocity. The inclination of the major principal stress ψ_σ can be calculated from

$$\psi_\sigma = \frac{1}{2}\arctan\left(\frac{2\sigma_{12}}{\sigma_{11}+\sigma_{22}}\right) \tag{5}$$

where σ_{ij} is the stress tensor. By choosing $\varsigma = \varphi$ (φ is the internal friction angle) and $\xi = \varphi - 2\chi$ (χ is the dilatancy parameter), Eq. (4) can be rewritten as

DOI: 10.1002/nag

$$\begin{aligned}(d_{11}+d_{22})\cos(\varphi-\chi) &= [(d_{11}-d_{22})\cos 2\psi_\sigma + 2d_{12}\sin 2\psi_\sigma]\sin(\chi)\\ 2(\Omega+w_{12})\sin(\varphi-\chi) &= [(d_{11}-d_{22})\sin 2\psi_\sigma - 2d_{12}\cos 2\psi_\sigma]\cos(\chi)\end{aligned} \tag{6}$$

For incompressible granular material undergoing planar flow ($\chi=0$), the kinematic behaviors can be theoretically described by the models with the following equations [20]:

$$\begin{aligned}d_{11}+d_{22} &= 0\\ 2(\Omega+w_{12})\sin\varphi &= (d_{11}-d_{22})\sin 2\psi_\sigma - 2d_{12}\cos 2\psi_\sigma\end{aligned} \tag{7}$$

As mentioned above, the angular velocity Ω has different interpretations in different kinematic models [17–19, 21]. In the double-shearing model [17], the angular velocity Ω is regarded as the rotation rate of the principal stress. In the double-sliding free-rotating model [18, 21], the angular velocity Ω is interpreted as the rotation rate of the sliding elements. In the DSR^2 model [19], the angular velocity Ω is identified with the average pure rotation rate (APR). In the monotonic or cyclic simple shear tests, a theoretical solution can be obtained for the angular velocity Ω. Therefore these kinematic models, except the double-sliding free-rotating model, can be evaluated by directly comparing the predicted values obtained from DEM tests with the theoretical angular velocity Ω. The theoretical angular velocity Ω in the double-sliding free-rotating model is indeterminate [21] and hence is evaluated using the method described below.

3.1. Theoretical rotation rate

By substituting Eq. (2a) or (2b) into Eq. (3b), the theoretical rotation rate Ω can be expressed as

$$\Omega = \left(\frac{\cos 2\psi_\sigma}{2\sin\varphi}+\frac{1}{2}\right)\dot{\theta} \tag{8}$$

where $\dot{\theta}$ is the rotation rate given by Eq. (2) and ψ_σ is the inclination of the major principal stress given by Eq. (5). It was found from biaxial compression tests that the residual frictional angle φ was 24.6° and 30.0° for $A_m=1.4$ and 1.7, respectively. For simplicity, an identical φ of 30° is used for all specimens. The theoretical rotation rate Ω was calculated using Eq. (8) during the DEM simple shear tests to evaluate the three kinematic models.

3.2. Double-shearing model

The double-shearing model regards the angular velocity Ω as the rotation rate of the major principal stress, i.e. $\dot{\psi}_\sigma$, which is defined as the increment of the principal stress inclination over a time interval Δt and calculated using

$$\dot{\psi}_\sigma = \frac{\psi_\sigma^{t+\Delta t}-\psi_\sigma^{t}}{\Delta t} \tag{9}$$

where ψ_σ^t is the principal stress inclination given by Eq. (4) at time t.

The double-shearing model will be evaluated by comparing $\dot{\psi}_\sigma$ with the theoretical rotation rate Ω given by Eq. (8).

3.3. Double-sliding free-rotating models

The double-sliding free-rotating model interprets Ω as the rotation rate of the sliding elements. Because the rotation of granular material is regarded as 'free', the rotation rate of the sliding elements is indeterminate. Therefore, De Josselin De Jong [21] stipulated the restriction of non-negative energy dissipation in each slip direction to apply this model to practical geo-engineering. For incompressible granular materials, Meharbadi and Cowin [47] further proposed an equivalent inequality to represent the requirement of non-negative energy dissipation as

$$A = 2|\Omega+w_{12}| < \frac{s_{km}e_{km}}{q\cos\varphi} = B \tag{10}$$

DOI: 10.1002/nag

where w_{12} is the spin tensor, q is the stress invariant defined by Eq. (11c), s_{km} and e_{km} are the deviatoric stress tensor and the deviatoric deformation rate tensor, respectively. In two-dimensions, the variables on the right hand side of inequality (10) can be calculated from the stress tensor σ_{ij} and the deformation rate tensor d_{ij} as

$$s_{ij} = \sigma_{ij} - \frac{1}{2}\delta_{ij}\sigma_{kk} \tag{11a}$$

$$e_{ij} = d_{ij} - \frac{1}{2}\delta_{ij}d_{kk} \tag{11b}$$

$$q = \frac{1}{2}\sqrt{(\sigma_{11}-\sigma_{22})^2 + 4\sigma_{12}^2} \tag{11c}$$

where δ_{ij} is the Kronecker delta. The internal friction angle φ is also chosen as 30° for consistency. The left hand side of inequality (10) can be obtained from the theoretical value of $\mathbf{\Omega}$ given by Eq. (8) and the spin tensor w_{12} is calculated by

$$w_{12} = \frac{1}{2}\left(\frac{\partial v_x}{\partial y} - \frac{\partial v_y}{\partial x}\right) = -\frac{1}{2}\dot{\theta} \tag{11d}$$

Therefore, the double-sliding free-rotating model will be evaluated by investigating inequality (10) in the DEM simple shear tests. Note that inequality (10) is derived in the framework of thermodynamics and thus the double-sliding free-rotating model can also be theoretically evaluated by examining the energy dissipation at all contacts during the numerical simulations. Because this paper focuses on the evaluation of the kinematic models through the angular velocity $\mathbf{\Omega}$ in the unified kinematic equations, the energy dissipation is not studied here for simplicity.

3.4. DSR^2 model for elliptical granular materials

In the DSR^2 model, the angular velocity $\mathbf{\Omega}$ is interpreted as the average pure rotation (APR) ω_3^c, which is defined based on the kinematic motions of contacting particles. In the previous work [19], the formulation of APR was proposed for circular particles and is extended for elliptical particles below.

Consider two particles m and n within a granular assembly composed of rigid elliptical particles, which deforms incrementally in the time interval from t to $t+\Delta t$. Particle m remains in contact with particle n over the time interval Δt, as shown in Figure 3. At time t, particles m and n translate at velocities $\dot{u}_{mi}^t$ and $\dot{u}_{ni}^t$ ($i=1, 2$), and rotate at the rates of $\dot{\theta}_m^t$ and $\dot{\theta}_n^t$, respectively. The corresponding translational and rotational accelerations are $\ddot{u}_{mi}^t$ and $\ddot{\theta}_m^t$, $\ddot{u}_{ni}^t$ and $\ddot{\theta}_n^t$, respectively.

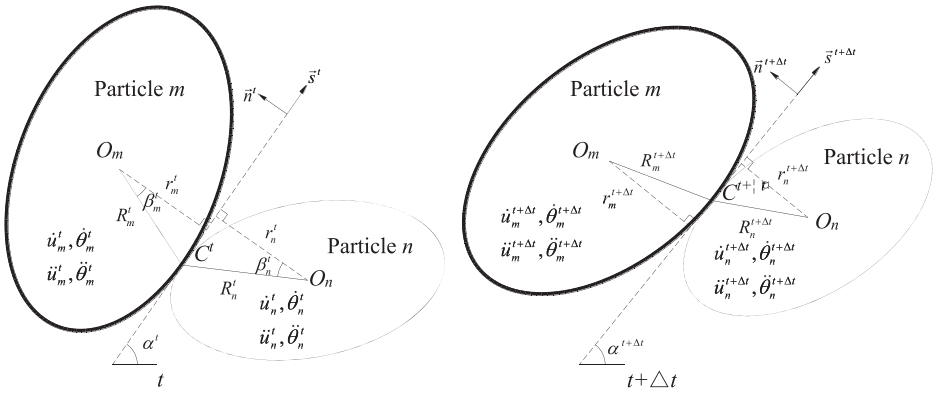

Figure 3. Kinematics of two ellipses in contact at times t and $t+\triangle t$.

DOI: 10.1002/nag

At time t, particles m and n rotate transiently with respect to contact C. The respective rotation radius, r_m^t and r_n^t, can be expressed as

$$r_m^t = R_m^t \cos\beta_m^t, \quad r_n^t = R_n^t \cos\beta_n^t \tag{12a}$$

where β_m^t and β_n^t are the angles shown in Figure 3(a), R_m^t and R_n^t are the contact radii measured from the center of particle m and n to the contact C, respectively. When the particles are circular, the relationship in Eq. (12a) becomes

$$r_m^t = R_m^t, \quad r_n^t = R_n^t. \tag{12b}$$

Over the time interval Δt, the tangential relative displacement between particle m and n at contact C can be obtained from

$$\Delta u_s = \int_t^{t+\Delta t} \dot{u}_s dt = \int_t^{t+\Delta t} \left[(\dot{u}_{mi} - \dot{u}_{ni}) s_i - \left(\dot{\theta}_m r_m + \dot{\theta}_n r_n \right) \right] dt \tag{13}$$

where the tangential vector $\vec{s} = (\cos\alpha,\ \sin\alpha)$ as illustrated in Figure 3(a).

Following the mean value theorem for integrals, the tangential relative displacement at contact C can be rewritten as

$$\Delta u_s = \dot{u}_s^{t+\lambda\Delta t} \cdot \Delta t \tag{14a}$$

where $0 < \lambda < 1$. The first order Taylor expansion of $\dot{u}_s^{t+\lambda\Delta t}$ yields

$$\dot{u}_s^{t+\chi\Delta t} = \dot{u}_s^t + \ddot{u}_s^t \cdot \lambda \Delta t \tag{14b}$$

where $\ddot{u}_s^t$ is the tangential relative acceleration. Therefore, the tangential relative displacement over the time interval Δt can be calculated as

$$\Delta u_s = \dot{u}_s^t \cdot \Delta t + \chi \cdot \ddot{u}_s^t \cdot (\Delta t)^2. \tag{14c}$$

Let us define the equivalent relative rotation $\Delta\theta_s$ caused by the tangential relative displacement Δu_s as follows:

$$\Delta\theta_s = \Delta u_s / r \tag{15}$$

where $r = 2r_m r_n / (r_m + r_n)$.

The equivalent relative rotation rate $\dot{\theta}_s$ can be expressed as

$$\dot{\theta}_s = \lim_{\Delta t \to 0} \frac{\Delta\theta_s}{\Delta t} = \frac{1}{r} \left[(\dot{u}_{mi} - \dot{u}_{ni}) s_i - \left(\dot{\theta}_m r_m + \dot{\theta}_n r_n \right) \right]. \tag{16}$$

Eq. (16) demonstrates that the equivalent relative rotation rate $\dot{\theta}_s$ at contact C consists of two components. The first component accounts for the tangential relative displacement resulting from the translation of the particles in contact. The second component accounts for the tangential relative displacement induced by their rotations. Similar to the definition of micro-pure rotation rate of circular particles [19], the micro-pure rotation rate of elliptical particles is defined as

$$\dot{\theta}^{pr} = \frac{1}{r} \left(\dot{\theta}_m r_m + \dot{\theta}_n r_n \right). \tag{17a}$$

Eq. (17a) indicates that the micro-pure rotation rate $\dot{\theta}^{pr}$ depends on the rotation rates of contacting particles and their transient rotation radius with respect to the contact point. Note that, although the derivation starts with elliptical particles, the aspect ratio does not appear explicitly in Eq. (17a). For circular particles, Eq. (12b) leads to

DOI: 10.1002/nag

$$\dot{\theta}^{pr} = \frac{1}{R}\left(\dot{\theta}_m R_n + \dot{\theta}_m R_n\right) \tag{17b}$$

where $R = 2R_m R_n/(R_m + R_n)$. Eq. (17b) is the micro-pure rotation rate defined for circular particles by Jiang et al. [19]. Hence, Eq. (17a) can be regarded as the generalized definition of the micro-pure rotation rate for granular materials.

For the whole granular assembly of elliptical particles, the average pure rotation rate (APR) can be calculated from

$$\omega_3^c = \frac{1}{N}\sum_{c=1}^{N}\dot{\theta}_c^{pr} = \frac{1}{N}\sum_{c=1}^{N}\frac{1}{r^c}\left(\dot{\theta}_m^c r_m^c + \dot{\theta}_n^c r_n^c\right) \tag{18}$$

where N is the total number of contacts. If a particle rotates counterclockwise, the rotation rate $\dot{\theta}_m$ is positive; otherwise, $\dot{\theta}_m$ is negative. Eq. (18) has been derived from the interaction of the contacting particles to calculate the APR of granular materials. Because the APR defined by Eq. (18) is a macroscopic quantity related to particle size as well as particle rotation, it can serve as an appropriate bridge between discrete micromechanics and constitutive modeling of granular materials. By interpreting the angular velocity $\boldsymbol{\Omega}$ as APR, the DSR^2 model becomes a hybrid model of discrete and continuum mechanics for non-coaxial granular materials.

In the numerical evaluations, the DSR^2 kinematic model will be examined by comparing APR calculated by Eq. (18) with the theoretical rotation rate $\boldsymbol{\Omega}$ given by Eq.(8).

4. DEM SIMULATION RESULTS

In this section, the DEM simple shear tests are first analyzed from the velocity fields and force distribution within the specimens. Then, the three kinematic models are evaluated by comparing the model predictions with the results observed in DEM monotonic simple shear tests. Finally, these models are further evaluated using the results obtained from DEM cyclic simple shear tests. Note that these kinematic models are evaluated based on macroscopic quantities defined over the specimens. Although averaging of these quantities may merge several quite different mechanisms, the evaluations are still reasonable because these models are proposed to predict the macroscopic behavior of granular materials, and this paper does not aim to discuss the mechanisms of non-coaxial behavior of granular materials.

4.1. Macro-mechanical response

Figure 4 presents the variation of the stress component on the non-rotated walls. The stress components were computed by integrating all the particle–wall contact forces over the corresponding wall. Figure 4(a) shows that, in both modes of shear tests, the vertical or horizontal

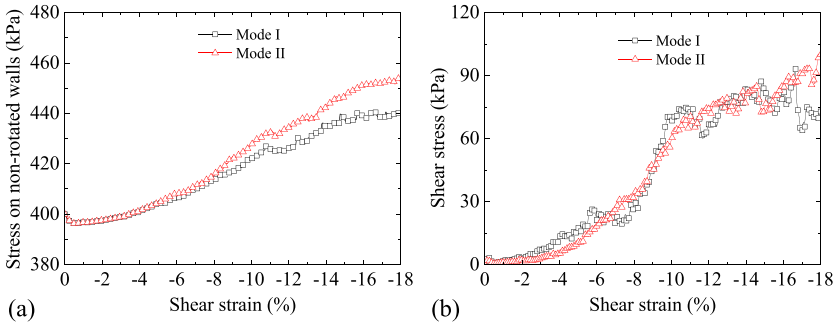

Figure 4. Stress components on the non-rotated walls during monotonic shear tests on medium-dense specimens: (a) vertical (horizontal) stress, (b) shear stress.

DOI: 10.1002/nag

stress on the non-rotated walls decreases slightly at first and then increases gradually to a value which is significantly larger than the initial stress. This indicates that the specimens tended to experience shear dilation at large strain after the initial contraction. Figure 4(b) shows that the shear stress component on the non-rotated walls increases gradually at first and then increases rapidly. The rate of increase of the stress components on the non-rotated walls decreases again when the shear strain exceeds 11%, which may result from the decreasing shear dilation rate.

4.2. Micro-analysis of simple shear tests

4.2.1. Velocity fields. Figure 6 presents the distributions of the average velocities in the x and y directions along the y-axis during the Mode I monotonic simple shear test on the medium-dense specimen with $A_m = 1.7$. The velocity fields were evaluated using the average velocities defined in a representative elementary area and the velocity vectors defined on each particle. The representative elementary area is referred to as a 'band' defined along the x- or y-axes, as shown diagrammatically in Figure 5. Because the band thickness plays an important role in measuring the void ratio of granular materials [43], several discretizations with different numbers of bands, i.e. 5, 9, 13 and 17, were used to calculate the average velocities. The band thickness decreased from 8.95 to 2.63 times the mean particle diameter d_{50}. Figure 6 shows that the measured average velocities in the x direction agree closely with the theoretical velocities estimated by Eq. (3a). In addition, there are only slight changes in the average velocities when the number of bands increases, which indicates that, within the investigated range, band thickness only slightly affects the description of the velocity field. It should be pointed out that, regardless of particle shape, specimen density or shear mode, the average velocities obtained from the simulations agree well with the theoretical solutions in all the monotonic simple shear tests. This demonstrates that the velocity field is well described by Eq. (2) and, therefore, the DEM simple shear tests performed are valid for the evaluation of the kinematic models.

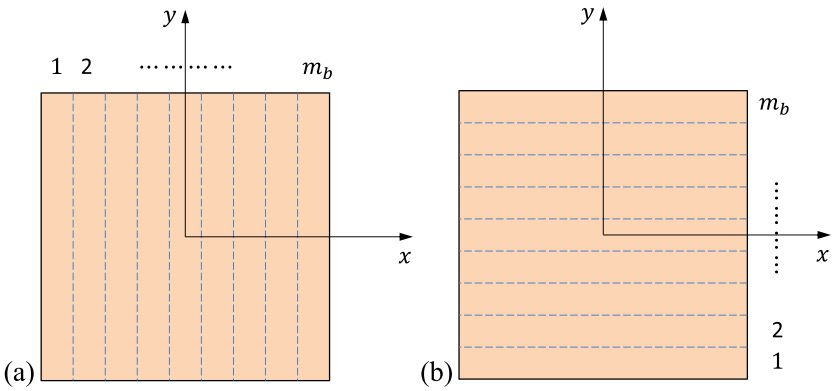

Figure 5. Bands to compute the average velocities: (a) bands along x-axis; (b) bands along y-axis.

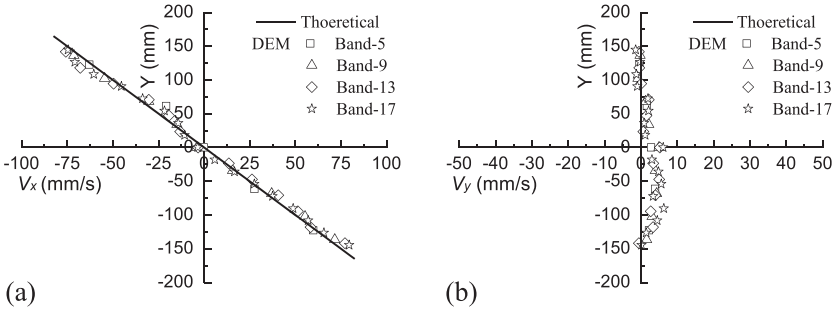

Figure 6. Average velocities along y-axis in Mode IDEM monotonic simple shear test on medium-dense granular specimen ($A_m = 1.7$): (a) velocity in x direction, (b) velocity in y direction.

DOI: 10.1002/nag

Figure 7 shows the complete velocity field corresponding to the average velocities shown in Figure 6. Here, the velocity field is defined for each particle as its displacement increment over the corresponding time interval. Figure 7 shows that the particles near the top and bottom walls move almost horizontally as described by Eq.(3a), while the particle near the center seem to rotate counter clockwise. However, as illustrated in Figure 7, the average vertical velocity near the specimen center is still close to zero because of the anti-symmetrical distribution of the velocity field. Hence, it can be generally summarized that Eq. (2) can properly describe the velocity field within granular specimens during DEM simple shear tests. Consequently, the theoretical rotation rate $\boldsymbol{\Omega}$ given by Eq. (8) can serve as an index to evaluate the above kinematic models.

4.2.2. Force distribution. Because the applied forces are transmitted within the granular assembly via the inter-particle contacts, the evolution of the transmission pathways of the strong forces, which are larger than their average value, usually controls the mechanical shear behavior of granular materials [48, 49]. Hence, the force distribution within the granular specimens during DEM simple shear tests is investigated here.

Figure 8 presents the transmission pathways of the strong forces via the interparticle contacts, i.e. the strong contact force network, at three different shear strains during DEM monotonic simple shear tests on the medium-dense specimens with $A_m = 1.7$. It should be pointed out that the strong contact force network illustrated in Figure 8 reflects the distribution of normal stress on the boundaries. Figure 8 shows that, in the Mode I simple shear test, the force network distributes preferentially in a direction inclined about 45° to the x-axis. In this case, the contact forces in the upper-right and lower-left zones are relatively larger than in other domains of the specimen. In contrast, in the Mode II simple shear test, the preferential direction of the force network is inclined at approximate $-40°$ to the x-axis. Correspondingly, the contact forces generally decrease in the upper-right and lower-left zones but increase in the upper-left and lower-right zones.

Figure 7. Velocity field in medium-dense specimen($A_m = 1.7$)during Mode I DEM monotonic simple shear test.

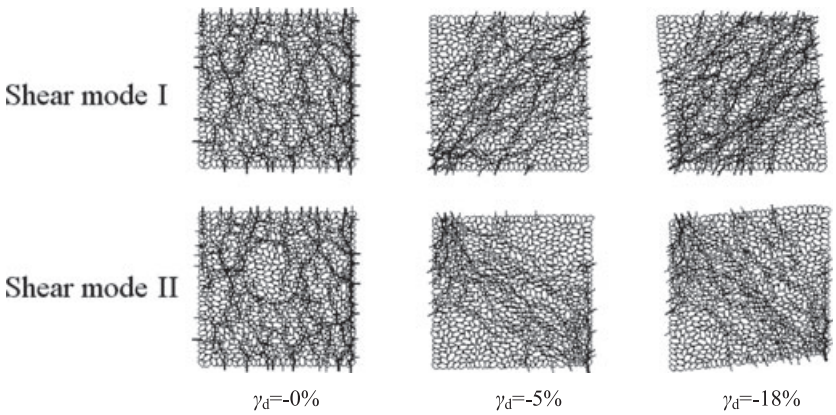

Figure 8. Strong force network in medium-dense granular specimens ($A_m = 1.7$) at different shear strains during DEM monotonic simple shear tests.

DOI: 10.1002/nag

As discussed above, Figure 8 demonstrates clearly that the force network is generally non-uniformly distributed, which results in the non-uniformity of boundary stresses during simple shear tests. It has been found that uniform boundary stresses cannot be achieved in either experimental or numerical simple shear tests. However, it was accepted that true simple shear conditions can be achieved in the central and large part of the specimens. In addition, experimental and numerical investigations into the macro- and micro-mechanical behavior of granular material have shown that the external forces are mainly resisted by the strong contact forces in the granular assembly rather than equally resisted by the contact force between each pair of contacting particles, which plays an important role in the non-uniformity of force network illustrated in Figure 8.

Figure 9 illustrates the orientation distribution of strong contact forces within the medium-dense specimens at the shear strains presented in Figure 8. Figure 9 shows that the orientation of the strong contact forces deviates significantly from the vertical direction after simple shearing commenced. In the simple shear stage, the orientation of strong contact forces is mainly in the range of $45 \pm 30°$ in Mode I simple shear tests and $-60 \pm 30°$ in Mode II simple shear tests. This confirms the observation made from Figure 8. In addition, Figure 9 shows that there are only slight changes in the orientation of strong contact forces when the shear strain increases from -5% to -18%. Note that the shear strain was treated as negative in DEM monotonic simple shear tests because the peak rotation rate $\dot{\theta}_0$ is positive and the sign convention of the kinematic models [17–21] is also employed in our DEM simulations. It should be pointed out that the fabric has not reached the steady critical state when the maximum shear strain is reached and that simple shearing should be continued to larger strain if the steady critical state is to be studied, which is not the focus of this paper.

Similar orientational distributions of the strong contact forces can be observed in the other DEM monotonic simple shear tests irrespective of particle shape, specimen density or shear mode. This suggests that these factors do not affect the numerical evaluations based on the DEM monotonic simple shear tests, as will be shown below.

4.3. Model evaluation in DEM monotonic simple shear tests

4.3.1. Double-shearing model. Figure 10 compares the theoretical rotation rates Ω with the rotation rates of the major principal stress $\dot{\psi}_\sigma$ obtained from the DEM monotonic simple shear tests on

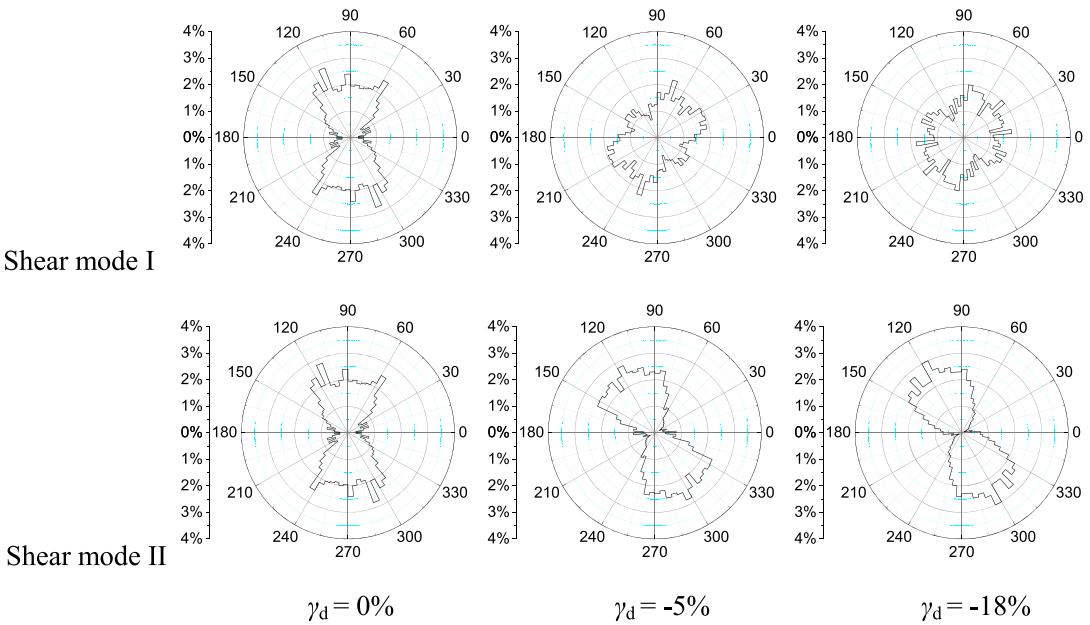

Figure 9. Strong contact force orientation in medium-dense granular specimens ($A_m = 1.7$)at different shear strains during DEM monotonic simple shear tests.

DOI: 10.1002/nag

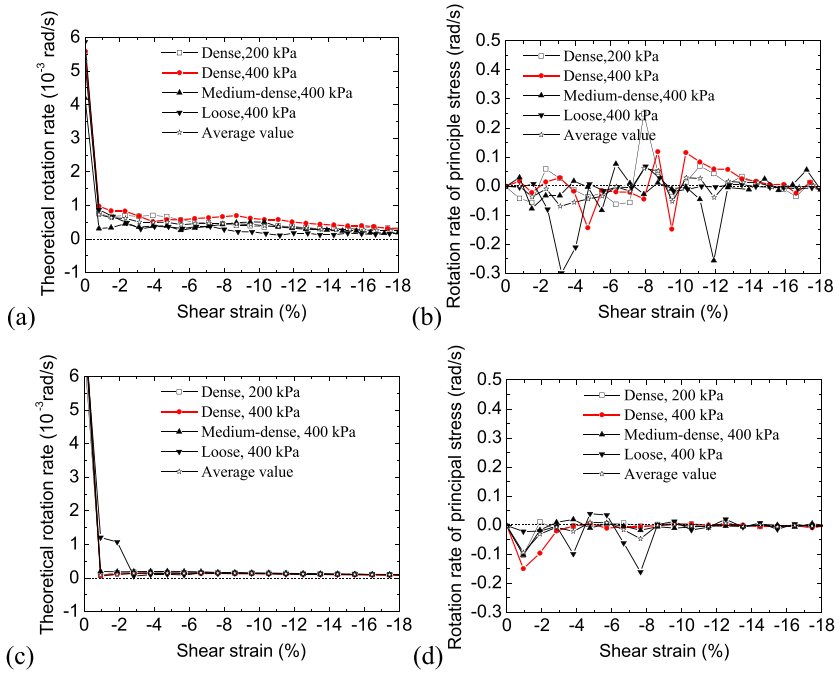

Figure 10. Theoretical rotation rates and rotation rates of the major principal stress in granular specimens ($A_m = 1.4$) during DEM monotonic simple shear tests: (a)(b) in Mode I, (c)(d) in Mode II.

elliptical particles with $A_m = 1.4$. Figure 10(a) shows that, in Mode I simple shear tests, the theoretical rotation rates Ω drop rapidly from 0.006 rad/s to 0.001 rad/s when the shear strain increases from 0% to −1.0%, and then reduces slowly to a very small positive value with the increasing shear strain. Figure 10(b), however, shows that the rotation rates of the major principal stress $\dot{\psi}_\sigma$ in Mode I simple shear tests fluctuate in the range between −0.3 and 0.3 rad/s. Hence, the rotation rates of the major principal stress $\dot{\psi}_\sigma$ differ quantitatively and qualitatively from the theoretical rotation rates Ω in Mode I monotonic simple shear tests. Figure 10(c) shows that, in Mode II monotonic simple shear tests, the theoretical rotation rates Ω drop from 0.006 rad/s to almost zero at a shear strain of −1.0% and then remain almost constant. Figure 10(d) shows that the rotation rates of the major principal stress $\dot{\psi}_\sigma$ in Mode II shear tests are in the range between −0.2 and 0.05 rad/s. Again, in Mode II monotonic simple shear tests, the rotation rates of the major principal stress $\dot{\psi}_\sigma$ are significantly different from the theoretical rotation rates Ω.

Figure 11 compares the theoretical rotation rates Ω with the rotation rates of the major principal stress $\dot{\psi}_\sigma$ obtained from the DEM monotonic simple shear tests on elliptical particles with $A_m = 1.7$. Comparing with Figure 10, Figure 11 shows that there are only slight changes in the values of Ω and $\dot{\psi}_\sigma$ when the aspect ratio increases from 1.4 to 1.7. In addition, Figure 11 also demonstrates the quantitative and qualitative differences between Ω and $\dot{\psi}_\sigma$ in both modes of simple shear tests, as already observed in Figure 10. Hence, the assumption $\Omega = \dot{\psi}_\sigma$ in the double-shearing model [17] appears to contradict the observations obtained from DEM monotonic simple shear tests.

The numerical simulations reveal that the main direction of the inter-particle contacts rotates gradually to coincide with the major principal stress, while the main direction of the contact forces is almost always consistent with the principal stress direction. This indicates that the non-coaxial behavior of granular material is related to the different rotation rates of the main directions of the inter-particle contacts and the contact forces. However, the double-shearing model relates the rotation rate only to the major principal stress, which probably accounts for the reason why the model predictions do not agree with the numerical results.

4.3.2. Double-sliding free-rotation models. Figure 12 presents quantities A and B in inequality (10) during DEM monotonic simple shear tests $A_m = 1.4$. Figure 12(a) shows that both quantities vary

DOI: 10.1002/nag

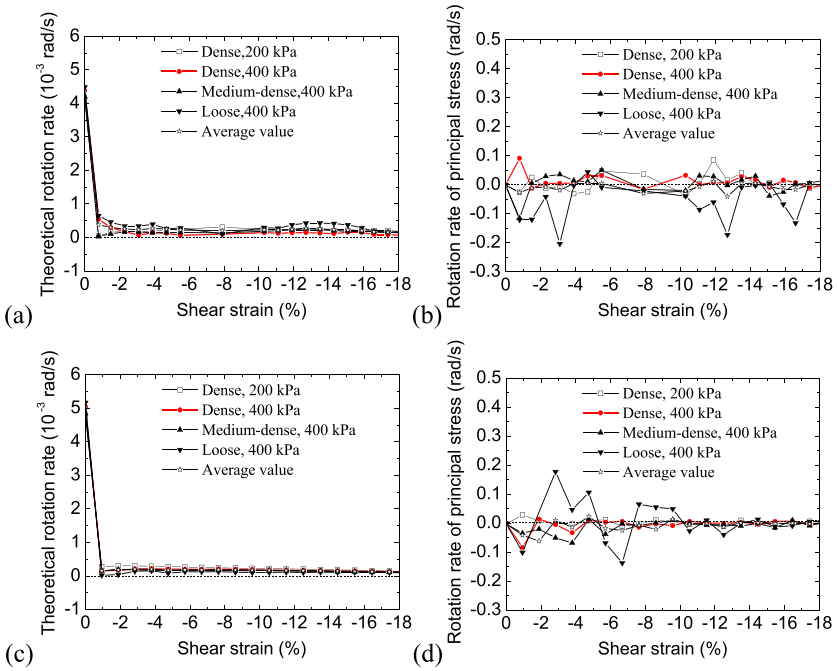

Figure 11. Theoretical rotation rates and rotation rates of the major principal stress in granular specimens ($A_m = 1.7$) during DEM monotonic simple shear tests: (a)(b) in Mode I, (c)(d) in Mode II.

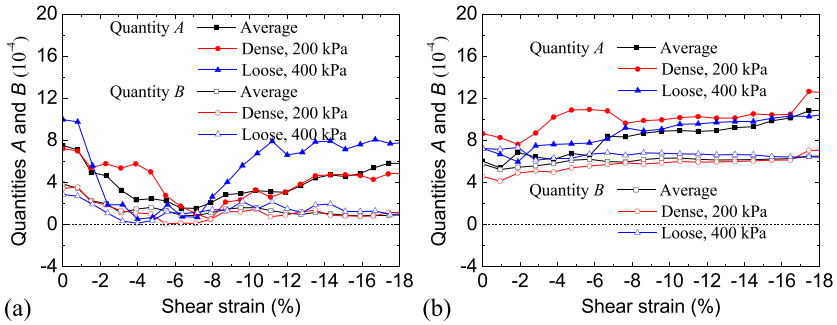

Figure 12. Measured quantities A and B in inequality (7) of granular specimens ($A_m = 1.4$) during DEM monotonic simple shear tests: (a) in Mode I, (b) in Mode II.

significantly during Mode I simple shear tests. In addition, quantity A is always positive but quantity B is almost zero at a shear strain of about -6%. In contrast, Figure 12(b) shows that both quantities are far larger than zero and tend to increase with shear strain during Mode II simple shear tests. Figure 12 demonstrates clearly that quantity A is generally larger than B in both modes, although their variations are different.

Figure 13 provides quantities A and B in inequality (10) during monotonic simple shear tests with $A_m = 1.7$. Figure 13(a) shows that, in Mode I, quantity A tends to increase while quantity B tends to decrease with increasing shear strain. In contrast, Figure 13(b) shows that both quantities tend to increase with increasing shear strain in Mode II. In addition, Figure 13 also demonstrates that $A > B$ during monotonic simple shear tests with $A_m = 1.7$.

The observations made from Figures 12 and 13 indicate that, irrespective of particle shape, specimen density or shear mode, quantity A is larger than B during monotonic simple shear tests. This is opposite to the assumption that quantity A should be smaller than B in the double-sliding free-rotation models. Therefore, the energy dissipation requirement in the double-sliding free-rotation models, as given by inequality (10), is not satisfied in DEM monotonic simple shear

DOI: 10.1002/nag

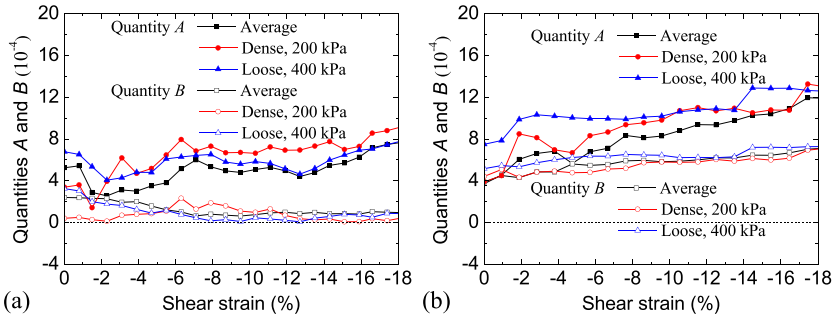

Figure 13. Measured quantities A and B in inequality (7) of granular specimens ($A_m = 1.7$) during DEM monotonic simple shear tests: (a) in Mode I, (b) in Mode II.

tests on elliptical granular materials. Hence, this requirement seems to be too strong to describe the kinematic flow of elliptical granular materials. This agrees with the remarks made by Mehrabadi and Cowin [47], as well as the theoretical analysis and numerical simulations reported by Jiang et al. [19, 37].

4.3.3. DSR^2 model. Figure 14 provides the theoretical rotation rates Ω obtained from DEM simulations using Eq. (8) and the APRs predicted by the DSR^2 model for the medium-dense granular specimens with $A_m = 1.4$. Figure 14 demonstrates that, despite slight differences, the APRs agree well with the theoretical rotation rates Ω in both modes, especially at large shear strain. In Mode I shear tests, as shown in Figure 14(a), Ω decreases gradually from 0.0008 rad/s to 0.0004 rad/s when the shear strain increases from 0 to -10%, and then remains almost constant. The APR is appear to be always constant around 0.0003 rad/s during Mode I simple shear tests. Figure 14(b) shows that Ω reduces slightly but steadily with increasing shear strain from an initial 0.0003 rad/s to 0.0001 rad/s, while the APRs fluctuate about 0.00015 rad/s in Mode II simple shear tests. It is worth mentioning that the APRs agree with the theoretical rotation rates Ω in other DEM monotonic simple shear tests on elliptical particle specimens ($A_m = 1.4$). This can be confirmed by the agreement between the average values of APR and Ω, as shown in Figure 14.

Figure 15 provides the theoretical rotation rates Ω obtained from DEM simulations using Eq. (8) and APRs predicted by the DSR^2 model for the medium-dense granular specimens with $A_m = 1.7$. Although both quantities in Mode II shear tests are slightly smaller than their respective counterparts in Mode I shear tests, Figure 15 still demonstrates the good agreement between APRs and Ω in monotonic simple shear tests, which confirms the observations made from Figure 14. Therefore, it can be concluded that, regardless of particle shape, the variable APR in the DSR^2 model [19] can be used to predict the angular velocity Ω of elliptical granular materials subjected to monotonic simple shear.

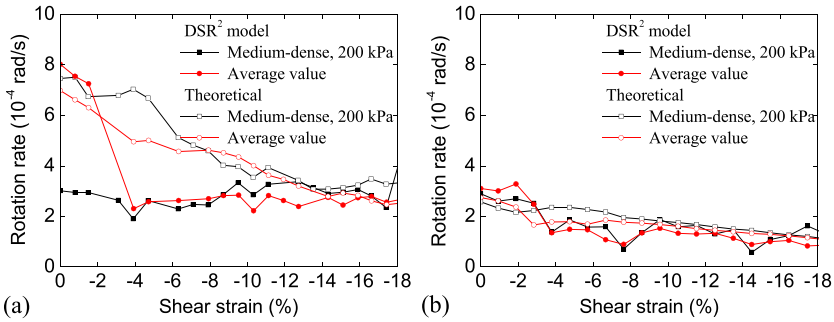

Figure 14. Theoretical rotation rates and APRs predicted by DSR2 model in medium-dense specimens ($A_m = 1.4$) during DEM monotonic simple shear tests: (a) in Mode I, (b) in Mode II.

DOI: 10.1002/nag

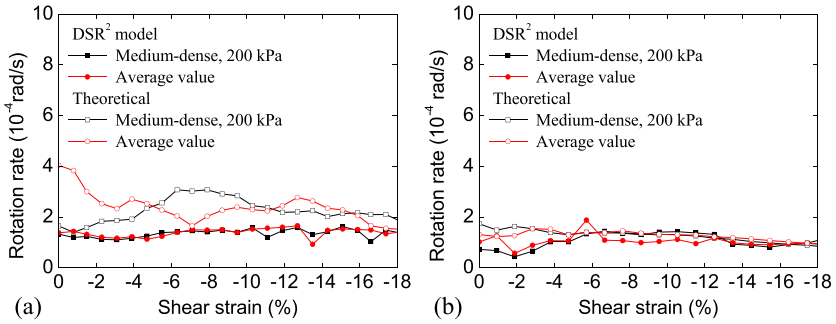

Figure 15. Theoretical rotation rates and APRs predicted by DSR2 model in medium-dense specimens ($A_m = 1.7$) during DEM monotonic simple shear tests: (a) in Mode I, (b) in Mode II.

4.4. Model evaluation in DEM cyclic simple shear tests

4.4.1. Double-shearing models. Figure 16 presents the inclination ψ_σ and the rotation rates $\dot{\psi}_\sigma$ of the major principal stress, as well as the theoretical rotation rates $\boldsymbol{\Omega}$ obtained from cyclic simple shear tests on the medium-dense specimens with $A_m = 1.4$. In Mode I cyclic shear tests, as shown in Figure 16(a), the inclination of the major principal stress changes periodically in the range between -50 and 50 during the cyclic simple shear tests. Figure 16(a) also shows that, in Mode I shear tests, the sign of $\dot{\psi}_\sigma$ is generally opposite to that of the theoretical rotation rates $\boldsymbol{\Omega}$, although both quantities undergo periodic variations between their respective maximum and minimum values. Note that the rotation rates of the major principal stress $\dot{\psi}_\sigma$ in Figure 16(a) have been scaled down by a reduction factor of 1/15, so the magnitude of $\dot{\psi}_\sigma$ is at least 15 times that of the theoretical rotation rates $\boldsymbol{\Omega}$. Hence, $\dot{\psi}_\sigma$ differs quantitatively and qualitatively from $\boldsymbol{\Omega}$ in Mode I DEM cyclic simple shear tests. The differences between $\dot{\psi}_\sigma$ and $\boldsymbol{\Omega}$ can also be observed in Mode II cyclic simple shear tests, as shown in Figure 16(b).

Figure 17 presents ψ_σ, $\dot{\psi}_\sigma$ and $\boldsymbol{\Omega}$ obtained from cyclic simple shear tests on the medium-dense specimens with $A_m = 1.7$. Figure 17 demonstrates clearly the evident differences between the

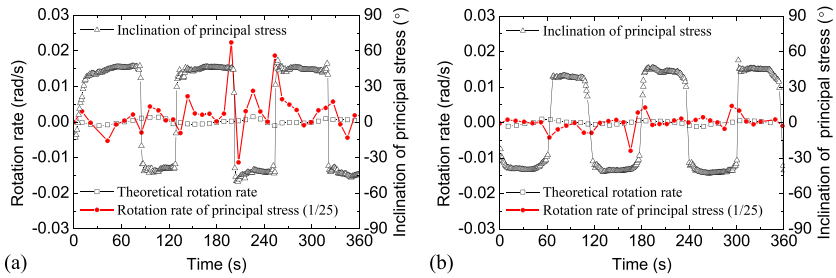

Figure 16. Rotation of the major principal stress and rotation rates during DEM cyclic simple shear tests on medium-dense specimens ($A_m = 1.4$): (a) in Mode I, (b) in Mode II.

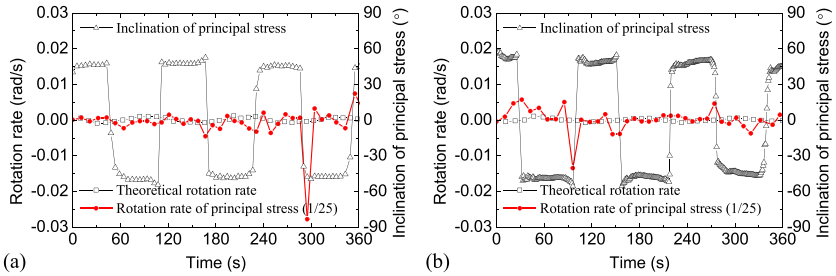

Figure 17. Rotation of the major principal stress and rotation rates during DEM cyclic simple shear tests on medium-dense specimens ($A_m = 1.7$): (a) in Mode I, (b) in Mode II.

DOI: 10.1002/nag

theoretical rotation rates Ω and the rotation rates of the major principal stress $\dot{\psi}_\sigma$ in cyclic simple shear tests. The rotation rates of the major principal stress $\dot{\psi}_\sigma$ are at least 25 and 10 times the magnitude of Ω in Mode I and II tests, respectively. It should be pointed out that such differences can be observed in other cyclic simple shear tests on specimens with $A_m = 1.4$ and 1.7, which is in agreement with the observations made in monotonic simple shear tests. Therefore, irrespective of particle shape, specimen density or shear mode, the assumption of $\dot{\vartheta} = \dot{\psi}_\sigma$ in the double-shearing model is not supported by the evidence obtained from monotonic or cyclic simple shear DEM simulations.

4.4.2. Double-sliding free-rotation models. Figure 18 provides quantities A and Bin inequality (10) during cyclic simple shear tests on the medium-dense specimens with $A_m = 1.4$. Figure 18 clearly shows that, regardless of shear mode, both quantities change periodically during cyclic simple shear tests and quantity A is generally larger than quantity B. As given by inequality (10), however, the double-sliding free-rotation models assume that the value of A should be smaller than B. This indicates that the energy dissipation described by inequality (10) is inconsistent with the observations obtained from DEM cyclic simple shear tests. Jiang et al. [19] have pointed out that particle rotation, which is intrinsic to most granular materials, plays an important role in the energy dissipation and that the energy dissipation rate is smaller than that calculated from the stress and plastic strain increment if particle rotation is considered. However, the energy dissipation requirement, i.e. inequality (10), was derived in a classical continuum mechanics framework without consideration of particle rotation. This can account for the inconsistency between the assumption given by inequality (10) and the data obtained from DEM simple shear tests. For specimens with $A_m = 1.7$, as shown in Figure 19, quantity A is also generally larger than quantity B during cyclic simple shear tests, which is again in contradiction to inequality (10). This confirms the observations made in the monotonic simple shear tests. Therefore, from the results obtained from DEM monotonic and cyclic simple shear tests, it can be concluded that the energy dissipation requirement given by inequality (10) in

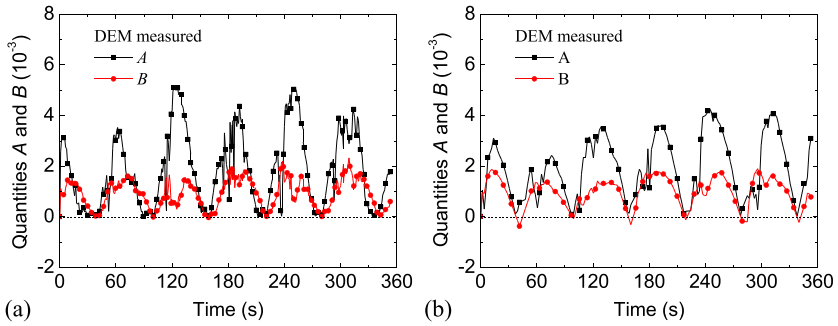

Figure 18. Measured quantities A and B in inequality (7) during DEM cyclic simple shear tests on medium-dense specimens ($A_m = 1.4$): (a) in Mode I, (b) in Mode II.

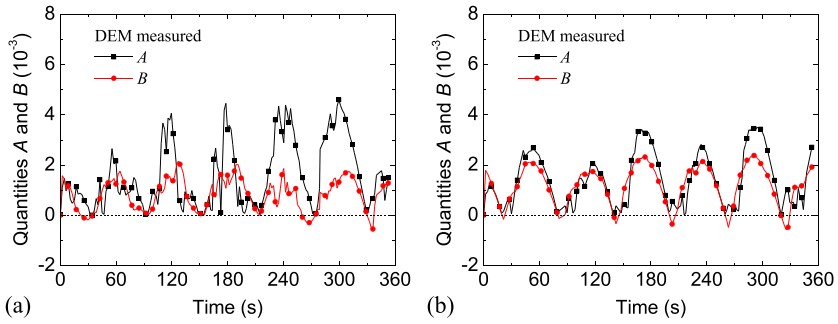

Figure 19. Measured quantities A and B in inequality (7) during DEM cyclic simple shear tests on medium-dense specimens ($A_m = 1.7$): (a) in Mode I, (b) in Mode II.

DOI: 10.1002/nag

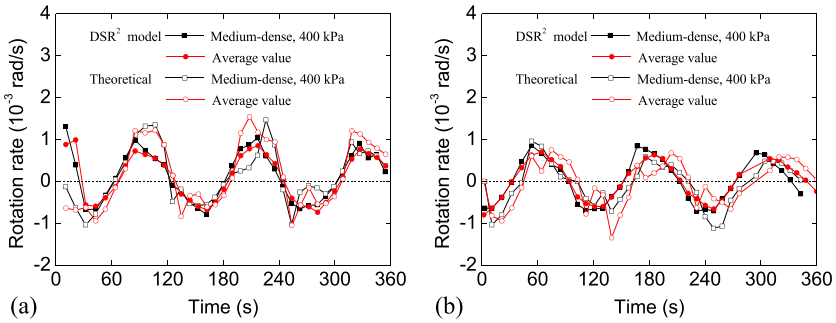

Figure 20. Theoretical rotation rates and APR predicted by DSR2 model during DEM cyclic simple shear tests on medium-dense specimens ($A_m = 1.4$): (a) in Mode I, (b) in Mode II.

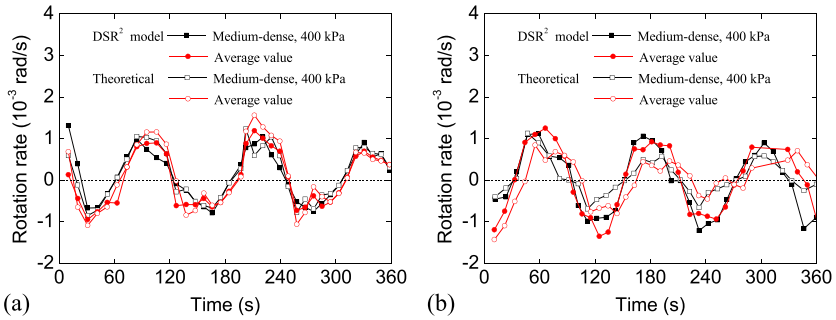

Figure 21. Theoretical rotation rates and APR predicted by DSR2 model during DEM cyclic simple shear tests on medium-dense specimens ($A_m = 1.7$): (a) in Mode I, (b) in Mode II.

the double-sliding free-rotation model is unduly restrictive as a constitutive assumption in describing the kinematic flow of elliptical granular materials.

4.4.3. DSR² model. Figure 20 compares the APRs predicted by the DSR^2 model with the theoretical rotation rates $\boldsymbol{\Omega}$ obtained from the DEM cyclic simple shear tests on specimens with $A_m = 1.4$. Figure 20 shows that, in both modes of cyclic simple shear tests, the APRs agree well with the theoretical rotation rates $\boldsymbol{\Omega}$. Both quantities vary periodically between -1.5×10^{-3} and 1.5×10^{-3}rad/s with identical periods during the cyclic simple shear tests, regardless of shear mode. In addition, the averaged APRs are qualitatively and quantitatively consistent with the averaged theoretical rotation rates $\boldsymbol{\Omega}$. Moreover, the agreement between APRs and the theoretical rotation rates $\boldsymbol{\Omega}$ can also be observed in the cyclic simple shear tests on specimens with $A_m = 1.7$, as shown in Figure 21. Hence, it can be summarized that it is reasonable to employ APR as the angular velocity $\boldsymbol{\Omega}$ in the unified kinematical model [20] and that the DSR^2 model can well describe the non-coaxial flow of elliptical granular materials.

5. CONCLUSIONS

This paper has evaluated numerically three kinematic models associated with the non-coaxiality of geo-materials by performing DEM simple shear tests on elliptical granular materials. The models examined are the double-shearing model, the double-sliding free-rotating model and the double slip and rotation rate model (DSR^2 model). The underlying assumptions of these models have been examined based on results obtained from strain-controlled DEM monotonic and cyclic simple shear tests in which the volume of the specimens was kept constant. Two different modes of simple shear tests were considered because the inherent anisotropy of granular specimens may influence the

DOI: 10.1002/nag

evaluation of the results. The following conclusions can be drawn from the observations obtained from the numerical simulations:

1. The assumption $\Omega = \dot{\psi}_\sigma$ in the double-shearing model is not supported by the numerical results obtained from DEM monotonic and cyclic simple shear tests on elliptical granular materials with different aspect ratios. This agrees with the remarks made by Jiang et al. [37, 50] based on numerical evaluations and theoretical analyses. However, the relationship $\Omega = \dot{\psi}_\sigma / m$ that appears to apply for discs [37, 50] does not apply for ellipses, the reason for this needs to be investigated in the future.
2. The requirement of energy dissipation in the double-sliding free-rotating model seems to be too strong to describe the kinematic flow of elliptical granular materials, which can be observed in all DEM simple shear tests irrespective of particle shape, specimen density or shear mode. This agrees with the observations made in the numerical and theoretical analyses of disc assemblies [37]. The non-coaxial behavior of granular material during shearing is related to changes to the inter-particle contacts and the contact forces. Hence, the double-shearing model and the double-sliding free-rotating model may be improved by incorporating the variables that reflect the changes to the inter-particle contacts and the contact forces.
3. The APRs predicted by the DSR^2 model are in good agreement with the theoretical rotation rates Ω in all DEM simple shear tests on elliptical granular materials. This is consistent with the conclusion in previous work [37, 51]. Hence, the concept of APR appears to be a reasonable variable to use in kinematic models, and the DSR^2 model is effective for describing the non-coaxial flow of both circular and elliptical particles.

In future works it is planned to further examine the three models by using 3D DEM [52, 53] under simple stress paths or complex stress paths [54, 55].

ACKNOWLEDGEMENTS

This work is funded by China National Funds for Distinguished Young Scientists with Grant No. 51025932, and the National Natural Science Foundation of China with No. 51579178. Support by the EU through FP7-PEOPLE-2011-IRSESGEOGAN294976 is also acknowledged. In addition, the authors would like to thank Dr. Colin Thornton, University of Birmingham, UK for his valuable comments on this paper.

REFERENCES

1. Drescher A, De Josselin De Jong G. Photoelastic verification of a mechanical model for the flow of a granular material. *Journal of the Mechanics and Physics of Solids* 1972; **20**(5):337–340.
2. Gutierrez M, Ishihara K, Towhata I. Flow theory for sand during rotation of principal stress direction. *Soils and Foundations* 1991; **31**(4):121–132.
3. Ishihara K, Towhata I. Sand response to cyclic rotation of principal stress directions as induced by wave loads. *Soils and Foundations* 1983; **23**(4):11–26.
4. Symes M, Gens A, Hight DW. Undrained anisotropy and principal stress rotation in saturated sand[J]. *Geotechnique* 1984; **34**(1):11–27.
5. Wong RKS, Arthur JRF. Sand sheared by stresses with cyclic variations in direction[J]. *Geotechnique* 1986; **36**(2):215–226.
6. Cai YY. An experimental study of non-coaxial soil behaviour using hollow cylinder testing. Nottingham: University of Nottingham, 2010.
7. Symes MJ, Gens A, Hight DW. Drained principal stress rotation in saturated sand. *Geotechnique* 1988; **38**(1):59–81.
8. Roscoe KH. The influence of strains in soil mechanics. *Geotechnique* 1970; **20**(2):129–170.
9. Joer HA, Lanier J, Fahey M. Deformation of granular materials due to rotation of principal axes. *Geotechnique* 1998; **48**(5):605–619.
10. Cai YY, Yu HS, Wanatowski D, *et al.* Non-coaxial behavior of sand under various stress paths. *Journal of Geotechnical and Geoenvironmental Engineering* 2012; **139**(8):1381–1395.
11. Luo Q, Wang ZT, Luan MT, *et al.* Factors analysis of non-coaxial constitutive model's application to numerical analysis of foundation bearing capacity. *Rock and Soil Mechanics* 2011; **32**(S1):732–737.
12. Muhlhaus H, Moresi L, Gross L, *et al.* The influence of non-coaxiality on shear banding in viscous-plastic materials [J]. *Granular Matter* 2010; **12**(3):229–238.
13. Cai YY, Yu J, Yang LT, *et al.* The review of experimental studies on non-coaxial soil behaviour using HCA. *Advanced Materials Research* 2012; **594**:46–49.
14. Yang YM, Yu HS. A kinematic hardening soil model considering the principal stress rotation. *International Journal for Numerical and Analytical Methods in Geomechanics* 2013; **37**(13):2106–2134.

DOI: 10.1002/nag

15. Hu P, Huang MS, Wu DG. Non-coaxial plasticity constitutive modeling of sands[J]. *Advanced Materials Research* 2013; **684**:150–153.
16. Qian J, Huang M, Sun H. Macro-micromechanical approaches for non-coaxiality of coarse grained soils. *Science China Technological Sciences* 2011; **54**(1):147–153.
17. Spencer AJM. A theory of the kinematics of ideal soils under plane strain conditions. *Journal of the Mechanics and Physics of Solids* 1964; **12**:337–351.
18. De Josselin De Jong G. The undefiniteness in kinematics for friction materials. Proceedings of the Conference on Earth Pressure Problem, Brussels: 1958; **1**:55–70.
19. Jiang MJ, Harris D, Yu HS. Kinematic models for non-coaxial granular materials. Part I: theory[J]. *International Journal for Numerical and Analytical Methods in Geomechanics* 2005; **29**(7):643–661.
20. Harris D. A unified formulation for plasticity models of granular and other materials. *Proceedings of the Royal Society of London* 1995; **A450**:37–49.
21. De Josselin De Jong G. The double sliding, free rotating model for granular assemblies. *Geotechnique* 1971; **21**(3):155–162.
22. Cundall PA, Strack ODL. The distinct numerical model for granular assemblies. *Geotechnique* 1979; **29**(1):47–65.
23. Tordesillas A, Walsh DC. Incorporating rolling resistance and contact anisotropy in micromechanical models of granular media. *Powder Technology* 2002; **124**(1):106–111.
24. Bardet JP, Proubet J. Numerical investigation of the structure of persistent shear bands in granular media. *Geotechnique* 1991; **41**(4):599–613.
25. Jiang MJ, Zhang WC, Sun YG, *et al.* An investigation on loose cemented granular materials via DEM analyses. *Granular Matter* 2013; **15**(1):65–84.
26. Jiang MJ, Yan HB, Zhu HH, *et al.* Modeling shear behavior and strain localization in cemented sands by two-dimensional distinct element method analyses. *Computers and Geotechnics* 2011; **38**(1):14–29.
27. Jiang MJ, Yu HS, Leroueil S. A simple and efficient approach to capturing bonding effect in naturally microstructured sands by discrete element method. *International Journal for Numerical Methods in Engineering* 2007; **69**(6):1158–1193.
28. Jiang MJ, Liu JD, Sun YG. Investigation into macroscopic and microscopic behaviors of bonded sands using the discrete element method. *Soils and Foundations* 2013; **53**(6):804–819.
29. Jiang MJ, Zhu HH, Harris D. Classical and non-classical kinematic fields of two-dimensional penetration tests on granular ground by discrete element method analyses. *Granular Matter* 2008; **10**(6):439–455.
30. Jiang MJ, Shen ZF, Zhu FY. Numerical analyses of braced excavation in granular grounds: continuum and discrete element approaches. *Granular Matter* 2013; **15**(2):195–208.
31. Jiang MJ, Murakami A. Distinct element method analyses of idealized bonded-granulate cut slope. *Granular Matter* 2012; **14**(3):393–410.
32. Jiang MJ, Yin ZY. Analysis of stress redistribution in soil and earth pressure on tunnel lining using the discrete element method. *Tunnelling and Underground Space Technology* 2012; **32**:251–259.
33. Arthur JRF, Koenders MA, Wong RKS. Anisotropy in particle contacts associated with shearing in granular media. *Acta Mechanica* 1986; **64**(1):19–29.
34. Li X, Yu HS. Numerical investigation of granular material behaviour under rotational shear. *Geotechnique* 2010; **60**(5):381–394.
35. Li X, Yu HS, Li XS. A virtual experiment technique on the elementary behaviour of granular materials with discrete element method. *International Journal for Numerical and Analytical Methods in Geomechanics* 2013; **37**(1):75–96.
36. Ai J, Langston PA, Yu HS. Discrete element modelling of material non-coaxiality in simple shear flows. *International Journal for Numerical and Analytical Methods in Geomechanics* 2014; **38**:615–635.
37. Jiang MJ, Harris D, Yu HS. Kinematic models for non-coaxial granular materials. Part II: evaluation. *International Journal for Numerical and Analytical Methods in Geomechanics* 2005; **29**(7):663–689.
38. Nouguier-Lehon C. Effect of the grain elongation on the behaviour of granular materials in biaxial compression. *Comptes Rendus Mecanique* 2010; **338**(10–11):587–595.
39. Yan G, Yu HS, Mcdowell G. Simulation of granular material behaviour using DEM. *Procedia Earth and Planetary Science* 2009; **1**(1):598–605.
40. Mahmood Z, Iwashita K. Influence of inherent anisotropy on mechanical behavior of granular materials based on DEM simulations. *International Journal for Numerical and Analytical Methods in Geomechanics* 2010; **34**(8):795–819.
41. Sazzad MM, Suzuki K. Micromechanical behavior of granular materials with inherent anisotropy under cyclic loading using 2D DEM. *Granular Matter* 2010; **12**(6):597–605.
42. Lin XS, Ng TT. Contact detection algorithms for three-dimensional ellipsoids in discrete element modelling. *International Journal for Numerical and Analytical Methods in Geomechanics* 1995; **19**(9):653–659.
43. Jiang MJ, Konrad JM, Leroueil S. An efficient technique for generating homogeneous specimens for DEM studies. *Computers and Geotechnics* 2003; **30**(7):579–597.
44. Fu PC, Dafalias YF. Study of anisotropic shear strength of granular materials using DEM simulation. *International Journal for Numerical and Analytical Methods in Geomechanics* 2011; **35**(10):1098–1126.
45. Oda M. Initial fabrics and their relations to mechanical properties of granular material. *Soils and Foundations* 1972; **12**(1):17–36.
46. Wong RKS, Arthur JRF. Induced and inherent anisotropy in sand[J]. *Geotechnique* 1985; **35**(4):471–481.

DOI: 10.1002/nag

47. Meharbadi MM, Cowin SC. On the double-sliding free-rotating model for the deformation of granular materials. *Journal of the Mechanics and Physics of Solids* 1981; **29**(4):269–282.
48. Azéma E, Radjai F, Saussine G. Quasistatic rheology, force transmission and fabric properties of a packing of irregular polyhedral particles. *Mechanics of Materials* 2009; **41**(6):729–741.
49. Antony SJ. Evolution of force distribution in three-dimensional granular media. *Physical Review E* 2000; **63**(1):11302.
50. Jiang MJ, Harris D, Yu HS. A novel approach to examining double-shearing type models for granular materials. *Granular Matter* 2005; **7**(3–4):157–168.
51. Jiang MJ, Yu HS, Harris D. Kinematic variables bridging discrete and continuum granular mechanics. *Mechanics Research Communication* 2006; **33**:651–666.
52. Jiang MJ, Shen ZF, Wang JF. A novel three-dimensional contact model for granulates incorporating rolling and twisting resistances. *Computers and Geotechnics* 2015; **65**:147–163.
53. Jiang MJ, Zhang FG, Thornton C. A simple three-dimensional distinct element modeling of the mechanical behavior of bonded sands. *International Journal for Numerical and Analytical Methods in Geomechanics* 2015; **39**(16):1791–1820.
54. Jiang MJ, Liu F, Shen ZF, Zheng M. Distinct element simulation of lugged wheel performance under extraterrestrial environmental effects. *Acta Astronautica* 2014; **99**:37–51.
55. Jiang MJ, He J, Wang JF, Liu F, Zhang WC. Distinct simulation of earth pressure against a rigid retaining wall considering inter-particle rolling resistance in sandy backfill. *Granular Matter* 2014; **16**(5):797–814.

DOI: 10.1002/nag